IOP Publishing | International Atomic Energy Agency Nuclear Fusion

Nucl. Fusion **57** (2017) 086005 (15pp) https://doi.org/10.1088/1741-4326/aa720c

Phase-space dependent critical gradient behavior of fast-ion transport due to Alfvén eigenmodes

C.S. Collins[1], W.W. Heidbrink[2], M. Podestà[3], R.B. White[3], G.J. Kramer[3], D.C. Pace[1], C.C. Petty[1], L. Stagner[2], M.A. Van Zeeland[1], Y.B. Zhu[2] and The DIII-D Team[1]

[1] General Atomics, PO Box 85608, San Diego, CA 92186-5608, United States of America
[2] University of California at Irvine, Irvine, CA 92697, United States of America
[3] Princeton Plasma Physics Laboratory, PO Box 451, Princeton, NJ 08543-0451, United States of America

E-mail: collinscs@fusion.gat.com

Received 1 March 2017, revised 13 April 2017
Accepted for publication 10 May 2017
Published 9 June 2017

Abstract

Experiments in the DIII-D tokamak show that many overlapping small-amplitude Alfvén eigenmodes (AEs) cause fast-ion transport to sharply increase above a critical threshold in beam power, leading to fast-ion density profile resilience and reduced fusion performance. The threshold is above the AE linear stability limit and varies between diagnostics that are sensitive to different parts of fast-ion phase-space. Comparison with theoretical analysis using the NOVA and ORBIT codes shows that, for the neutral particle diagnostic, the threshold corresponds to the onset of stochastic particle orbits due to wave-particle resonances with AEs in the measured region of phase space. The bulk fast-ion distribution and instability behavior was manipulated through variations in beam deposition geometry, and no significant differences in the onset threshold outside of measurement uncertainties were found, in agreement with the theoretical stochastic threshold analysis. Simulations using the 'kick model' produce beam ion density gradients consistent with the empirically measured radial critical gradient and highlight the importance of including the energy and pitch dependence of the fast-ion distribution function in critical gradient models. The addition of electron cyclotron heating changes the types of AEs present in the experiment, comparatively increasing the measured fast-ion density and radial gradient. These studies provide the basis for understanding how to avoid AE transport that can undesirably redistribute current and cause fast-ion losses, and the measurements are being used to validate AE-induced transport models that use the critical gradient paradigm, giving greater confidence when applied to ITER.

Keywords: energetic particles, fast-ion transport, Alfvén eigenmodes, critical gradient

(Some figures may appear in colour only in the online journal)

1. Introduction

In tokamaks, Alfvén eigenmodes can exchange energy with fast-ions through resonant mode-particle interactions, causing fast-ions to move away from the core of the plasma. Redistribution of fast ions can affect the plasma profiles, beam deposition, and current drive, and losses induced by AE transport can lead to localized heating that can damage the vessel walls [1]. Multiple, small-amplitude AEs are expected to be destabilized in ITER, where alpha losses must be less than $\mathcal{O}(5\%)$ to avoid excess heat load of the first wall [2]. In DIII-D, significant fast-ion transport due to AEs has been observed in high $q_{\min}$ steady-state reactor scenarios where the measured neutron rate approaches 60% of the classical rate

predicted by the TRANSP NUBEAM code [3] assuming no anomalous transport, limiting the achievable β_N. Some scenarios with q_{min} closer to one still have AE activity, yet fast ions behave classically [4, 5]. Therefore, understanding the regimes where AEs lead to losses and reduced fusion performance is important for developing a practical long-pulse fusion power plant.

A vast literature exists on the transport of fast ions by AEs. In the first comprehensive theoretical study, Sigmar *et al* [6] followed alpha orbits with a Hamiltonian guiding center code ORBIT in the presence of toroidicity induced Alfvén eigenmodes (TAEs) that were computed by ideal MHD. They concluded that orbit stochasticity becomes important for field perturbations $\delta B/B \sim 10^{-3}$ and that losses are dominated by alphas that transition from passing orbits to unconfined banana orbits. A few years later, Berk *et al* [7] emphasized the potential importance of intermittent 'avalanche' events, where fast ions transported radially by one mode steepen the gradient elsewhere, destabilizing additional modes. More recently, Schneller *et al* [8] stressed that fast ions with large orbits can intersect multiple AEs, dramatically altering their transport. In experiment, the first observation of AE-induced damage of the walls was caused by convective losses near the midplane of DIII-D [9]. A few years later, tail ions that were transported by TAEs onto ripple-loss orbits damaged the vacuum vessel in TFTR [10]. Darrow *et al* [11] used a scintillator probe to measure the losses of RF-accelerated fast ions by TAEs on TFTR, confirming the importance of lost banana orbits. On JET, the importance of overlapping resonances was confirmed when orbit-following calculations showed that the observed TAEs with different toroidal mode numbers could account for the reductions in the gamma-ray signal from MeV RF tail ions [12]. Shortly thereafter, measurements of the profiles of beam ions in DIII-D [13] and JT-60U [14] showed that AEs flatten the fast-ion profile. Using AE eigenfunctions based on DIII-D experimental measurements, White *et al* [15] showed that the multiple AEs produce stochastic orbits that flatten the fast-ion profile, as experimentally observed. Meanwhile, García–Mu noz *et al* [16] observed coherent oscillations in a loss-detector signal at AE-mode frequencies in ASDEX-Upgrade. Transport and losses of fast ions by TAEs have also been measured on LHD [17, 18], CHS [19], NSTX [20, 21], MAST [22], and Globus-M [23].

Recent DIII-D experiments extend previous studies in two ways. First, a modulated neutral-beam source probes the incremental fast-ion transport [24]. Second, a systematic power scan in conjunction with the modulated source has shown that the threshold for appreciable transport coincides with the onset of orbit stochasticity [25], as theoretically predicted [6]. The observed behavior is consistent with the paradigm of a 'critical gradient,' with negligible transport below threshold and rapidly increasing transport above threshold [25, 26]. The primary purpose of this paper is to provide additional details about the critical transport threshold first reported in [25]. New power scans are presented to study the effects of altering the fast ion distribution function by varying the beam deposition geometry and altering the types of AEs present through electron cyclotron heating. This work shows that while the theoretical stochastic transport threshold is in good agreement with the measured threshold, proper quantitative comparisons of transport stiffness above threshold will require analysis beyond linear interpretation, because nonlinear AE amplitude modulation causes transport of both the modulated and bulk fast-ion distribution. The magnitude of critical gradient transport depends on given plasma conditions and AE activity; measurements show that the fast ion density increases in TAE-dominant cases compared to mixed AE cases, and simulations of the time-evolved transported fast-ion distribution function for above-threshold cases with mixed AE mode types show that the peak radial critical gradient of the beam density changes as the AEs and plasma conditions evolve in time. A companion paper [26] focuses further on fast-ion transport well above the transport threshold.

These measurements provide insights into the underlying physics mechanisms governing fast-ion transport and are being used in validation studies to develop a predictive, phase-space dependent AE transport model. An outstanding problem in energetic particle physics is to efficiently calculate AE-induced transport and the resulting fast-ion profile over a wide parameter regime. Critical gradient models may bypass the need for expensive nonlinear calculations of AE saturated amplitudes, instead utilizing easier calculations of linear stability. An early implementation of a critical gradient model [27] assumed that if the fast-ion gradient $\partial\beta_{EP}/\partial r$ exceeds the stability threshold of the fastest growing mode, then fast-ion transport becomes large, and particles are transported to flatten the profile and maintain marginal stability. Another early model [28, 29] uses a threshold associated with microturbulence that exceeds the linear stability threshold. The measurements reported here and in [25] show that the onset of significant fast-ion transport exceeds the linear AE stability threshold and is associated with the presence of multiple, overlapping AEs that cause particle orbits to become stochastic.

Here, we begin with details of the perturbative AE transport experiments in section 2, and the analysis technique to quantify fast ion transport is described in section 3. The measurements in section 4 show that the stiff transport threshold exceeds the linear threshold for AE stability, and the threshold varies between fast-ion diagnostics because different diagnostics measure different parts of phase space. Varied beam geometry is used to change the bulk fast-ion distribution and alter the total AE amplitude, and electron cyclotron heating is used to change the types of AEs present in the experiment, which increases the measured peak fast-ion density. In section 5, we present a theoretical analysis to understand how the measured transport levels are affected when the AE activity is varied with different beam geometry. It is found that stochastic orbit analysis is useful for determining the critical gradient threshold in phase-space if mode amplitudes are known. However, a simple relation between the total number of stochastic orbits and the measured stiffness is not straightforward. The paper is summarized in section 6.

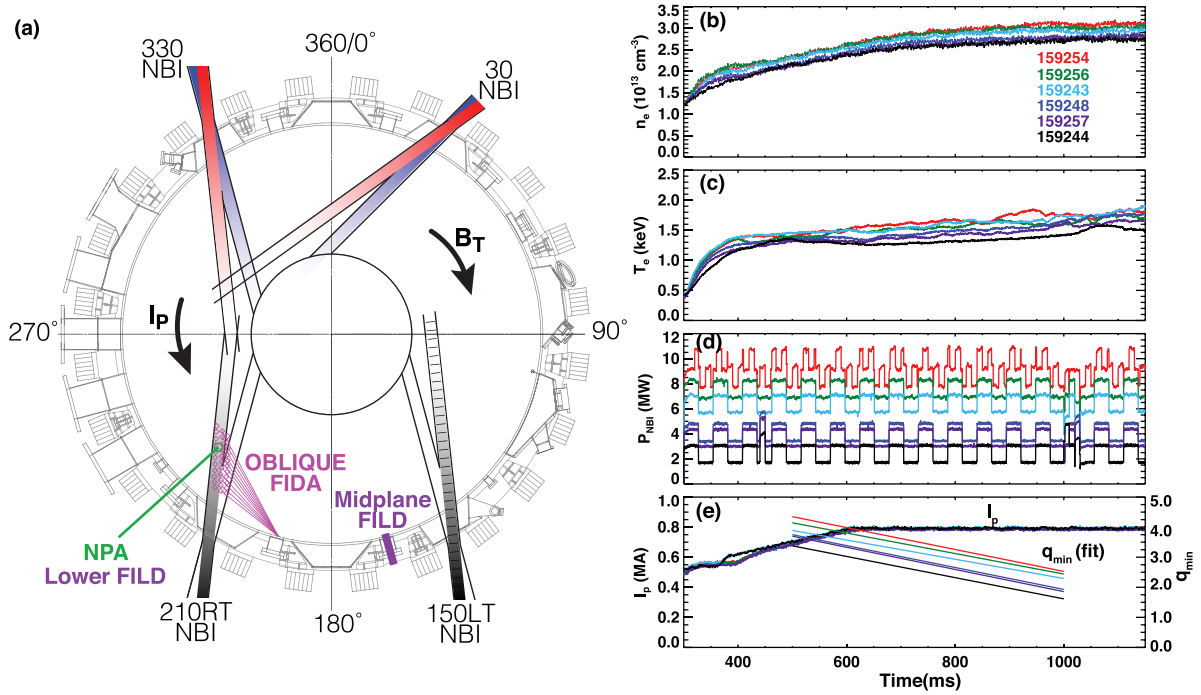

Figure 1. (*a*) Topview of DIII-D neutral beams and fast-ion diagnostics, and a comparison of discharges for different total beam powers with time histories of (*b*) density, (*c*) core electron temperature, (*d*) injected neutral beam power, and (*e*) plasma current and q_{min}. Here, q_{min} is based on an analytic model.

2. Critical gradient experiments at DIII-D

Experiments to measure AE-induced fast-ion transport were conducted in the current ramp phase of a DIII-D inner wall limited, oval-shaped, low-confinement (L-mode) plasma with $B_T = 2.05$ T. A topview of machine geometry and a comparison of discharge parameters for a representative set of shots is shown in figure 1. In these discharges, AEs are readily excited using early neutral beam injection beginning at $t = 300$ ms. The total AE activity is varied from shot-to-shot by changing the total neutral beam injected power from 2–9 MW using 70–80 kV neutral beams at 30° and 330° with various duty cycles (referred to as source beams in this paper). The primary 70 kV beam at 210° is on continuously except from $t = 1020$–1030 ms for diagnostic purposes. Gas feedback is used to control the target density to obtain similar parameters for each shot, though the varied heating power results in some variation in the core electron temperature, $T_e \approx 1.3$–1.7 keV, and line-averaged density, $n_e \approx 2.5$–2.9×10^{13} cm^{-3}. Electron temperature and density profiles are measured by the Thomson Scattering diagnostic. The 40-channel electron cyclotron emission (ECE) diagnostic [30] is used to measure electron temperature and the radial structures of AE induced temperature fluctuations at the midplane. Alfvén activity is also measured with the CO_2 laser interferometer for line-averaged density fluctuations, and external Mirnov coils are used to measure magnetic fluctuations and characterize toroidal mode numbers, typically up to $n = 6$. Ion temperature profiles are inferred from charge exchange recombination spectroscopy (CER), along with plasma toroidal rotation velocity (which reaches ≈60 km s^{-1}, corresponding to 6 kHz rotation frequency) and carbon impurity density (reaching 1×10^{12} cm^{-3} in the highest beam power discharges). Motional stark effect (MSE) measurements of the internal poloidal magnetic field are taken at the beam blips at $t = 440$ ms and $t = 1020$ ms in the lowest power discharges and in scans which use only perpendicular beam injection but are otherwise available and used to constrain the current profile in EFIT equilibrium reconstructions.

In all of the discharges, the plasma current ramps to $I_p = 800$ kA at 600 ms, and the magnetic safety factor (q) profile is reversed-shear in the time region of interest between $t = 500$–900 ms. Cascades of reverse shear Alfvén eigenmodes (RSAEs) appear when the minimum in the safety factor, q_{min}, crosses an integer value. The RSAEs are spatially localized around q_{min} and almost always sweep up in frequency. In figure 1(*e*), the evolution of q_{min} was determined by using the ad hoc model described in [31] to fit the frequency evolution of the RSAEs measured by the ECE spectrograms. The position of q_{min} is inferred from the maximum of RSAE magnitude in the cross-power spectrum between adjacent ECE channels. The minimum occurs at normalized minor radius $\rho_{qmin} \approx 0.2$–0.45, and ρ_{qmin} generally shifts inward in time and comparatively inward for lower total beam powers.

Several techniques were used to alter the amplitude, total number, and particular types of AEs. Power scans were conducted using source beams with more tangentially-directed injection (red shaded beams in figure 1(*a*)) or with more perpendicular-directed injection (blue shaded beams in figure 1(*a*)), while combinations of beams were used to achieve highest total beam powers. Altering the beam injection geometry changes the fast ion distribution function, and therefore changes the AE drive and resulting mode spectra. Figures 2(*a*) and (*b*) compares two discharges with the same

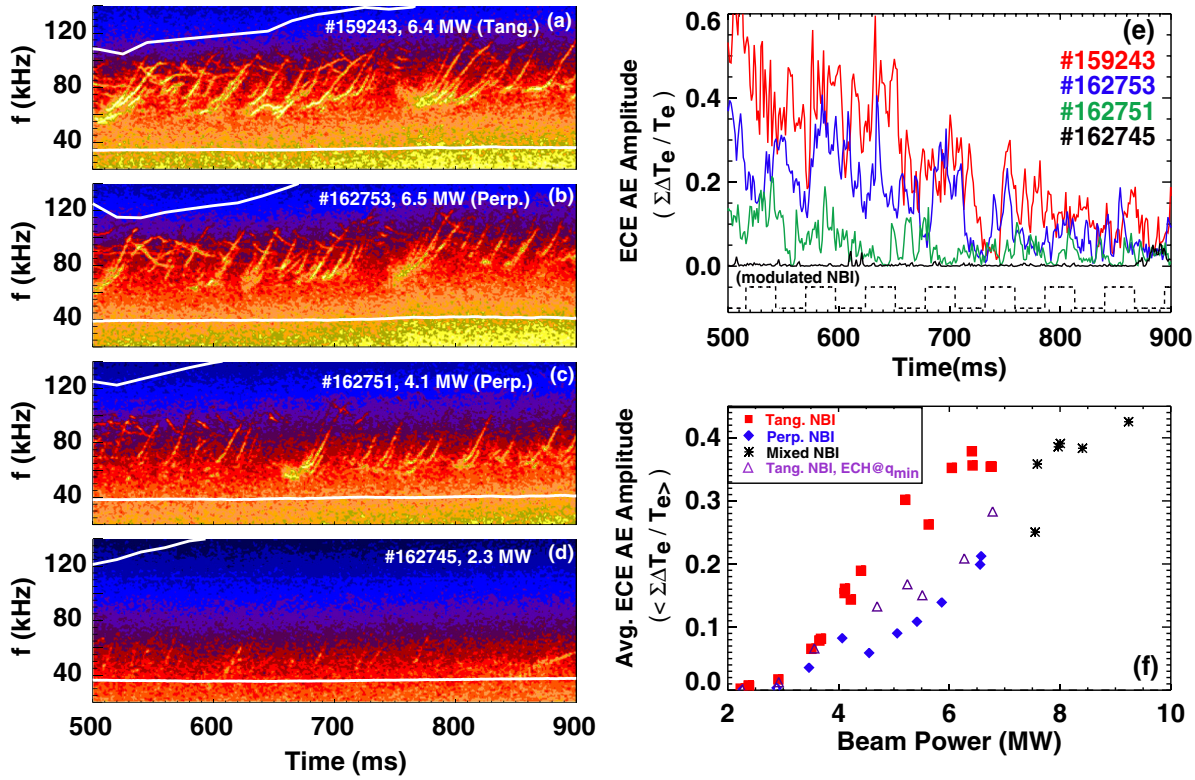

Figure 2. Examples of ECE data used to determine total AE activity. Total composite spectrograms using all ECE channels are shown in (*a*) thru (*d*). The white lines illustrate the AE frequency window based on the geodesic acoustic and TAE frequencies (typically 60–150 kHz). In (*a*), 6.4 MW tangential beam injection produces frequency-sweeping RSAEs and near constant frequency TAEs. In (*b*), perpendicular beam injection with similar power as (*a*) produces similar but weaker amplitude modes. In example (*c*), lower beam power produces less mode activity, where TAEs generally only exist earlier in the discharge, while the lowest beam power setting in (*d*) produces very little mode activity. In (*e*), the time history of the ECE AE amplitude is found by summing the total composite ECE spectrogram over the AE frequency window marked by the white lines in (*a*) thru (*d*). In (*f*), the ECE AE amplitude is time-averaged over a select number of periods and plotted versus total injected beam power for power scans using tangential beams (red squares), perpendicular beams (blue diamonds), mixed beams (black asterisks), and tangential beams with 3.2 MW ECH power at $q_{\min}$ (purple triangles).

total source beam power but different injection geometry. Tangential beam injection was found to increase the total AE amplitude and the total number of AEs compared to perpendicular beam injection for a given beam power. Lowering the total beam power decreases the mode activity, with very little mode activity appearing at the lowest total beam powers (figures 2(*c*) and (*d*)). Figure 2(*e*) shows that AE power decreases in time as parameters evolve in the discharge. The discharge generally evolves from a mix of both frequency sweeping RSAEs and near-constant frequency toroidicity induced Alfvén eigenmodes (TAEs), with fewer TAEs appearing later in time. Finally, the tangential beam power scan was repeated with the addition of injecting 3.2 MW of radially launched, 110 GHz electron cyclotron heating (ECH) power deposited near $q_{\min}$. Higher central electron temperature causes a delay in the current penetration to the axis, increasing the central safety factor profile inward from ρ_{qmin}. The local increase in electron temperature and safety factor alters the AE continuum, resulting in a TAE-dominant spectrum, as described in [31]. A comparison of the time-averaged AE amplitude versus beam power for all of the beam power scans discussed in this paper is shown in figure 2(*f*).

A variety of fast-ion diagnostics are used to quantify the fast ion population in different parts of fast-ion phase space, which has a complicated multi-dimensional dependence on variables such as energy, pitch ($v_{\|}/v$), and position. One way of visualizing diagnostic sensitivities is to plot the diagnostic 'weight functions' in orbit topology space, where different types of fast-ion orbits are classified in the magnetic moment versus toroidal canonical angular momentum plane (see figure 3(*a*)). The solid state neutral particle analyzer (NPA) [32] measures escaping fast neutrals resulting from charge exchange and is sensitive to trapped fast ions that have a narrow range in pitch and broad range in energy. The fast-ion deuterium alpha (FIDA) [33] diagnostic records a spectrum of line-integrated, Doppler-shifted light emissions resulting from fast-ion charge exchange collisions with a neutral beam and is sensitive to a broad range of co-passing fast ions (figure 3(*b*)). In this paper, the FIDA brightness is found by integrating the spectra over a wavelength range which corresponds to a line-of-sight energy range of 21.0–61.3 keV. The diagnostic beam is turned off from $t = 1020 - 1030$ ms to enable a background-subtracted equilibrium 'FIDA density' profile for comparison to the FIDASIM code [34]. The neutron diagnostics [35] measure the neutron emission rate primarily from beam-plasma deuterium-deuterium fusion reactions, and signals represent the total number of high energy fast ions over a large volume, with increased sensitivity to counter-passing orbits. Finally,

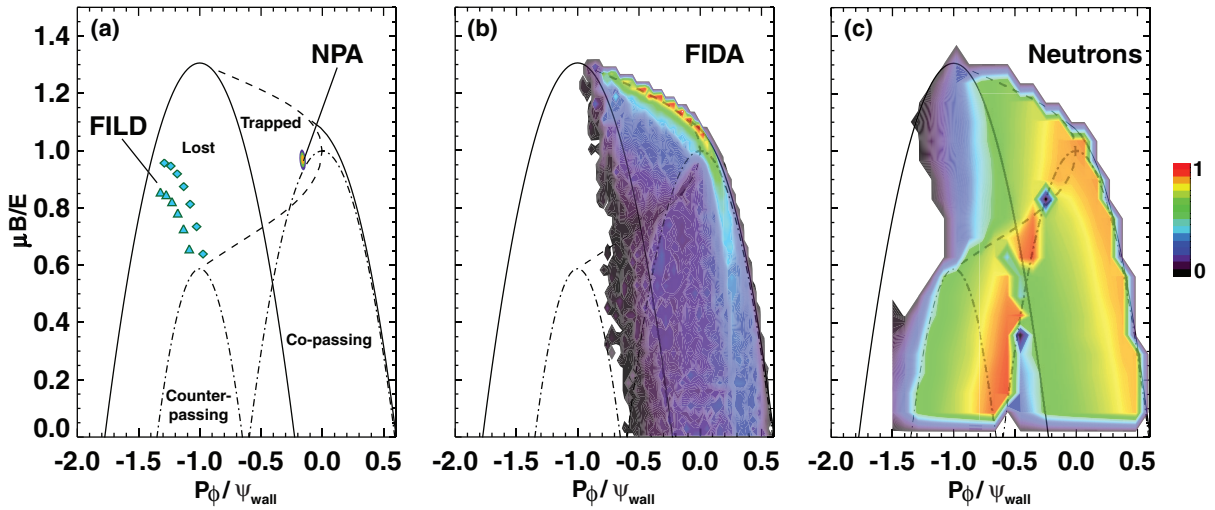

Figure 3. Fast ion orbit classification and visualization of the various regions of measurement sensitivity in orbit topology space for (*a*) FILD (at $E = 80$ keV) and NPA (integrated over all energies), (*b*) FIDA (integrated over line-of-sight energy range 20–80 keV), and (*c*) neutron diagnostic (at $E = 75$ keV). The weight functions were calculated for shot 159243 at $t = 790$ ms and color red is the normalized maximum value for each diagnostic.

the fast-ion loss detector [36] (FILD) records fast ions on loss orbits near the machine wall with high time resolution (figure 3(*a*)). Separate detectors are located at the midplane and 45 degrees below the midplane.

3. Transport analysis

In order to measure incremental transport, the fast-ion pressure profile is modulated with a period of either 50 ms or 54 ms using a 1.4 MW, 70 kV, off-axis neutral beam at 150°. This was found to produce an adequate population of 'test' particles across phase space and is less likely to (undesirably) drive AE activity compared to on-axis beam injection. The modulated population of particles appears on the FIDA signals as a triangle-shaped waveform that becomes distorted at high total beam power. Signal response and quantification of incremental fast-ion transport using a novel analysis method is described in detail in [24]. First, the data is detrended by subtracting the signal smoothed using a boxcar average window equal to the modulation period in order to isolate the modulated response from the slowly evolving background signal. Single waveforms can be analyzed for diagnostics with good signal-to-noise ratio and shots with steady source beams. To improve the signal-to-noise ratio, the detrended signal is conditionally averaged over several periods, beginning at $t = 500$ ms or $t = 516$ ms. It is important to note that the source beams used to drive AEs in the experiment are not necessarily steady: they are modulated at 1/4, 1/3, 1/2, or 2/3 duty cycles to achieve the desired total beam power. Thus, the number of periods used for the conditional averaging varies from shot to shot to average out the source power, so that the detrended, conditionally averaged beam power is a constant amplitude, modulated beam square wave (which is positive in the first half cycle and negative in the second half). Figure 4 shows a comparison of detrended, conditionally averaged signals for two different beam power shots; a low power, 2.4 MW shot with very little AE activity, and a high power 8.0 MW shot with prevalent AE activity.

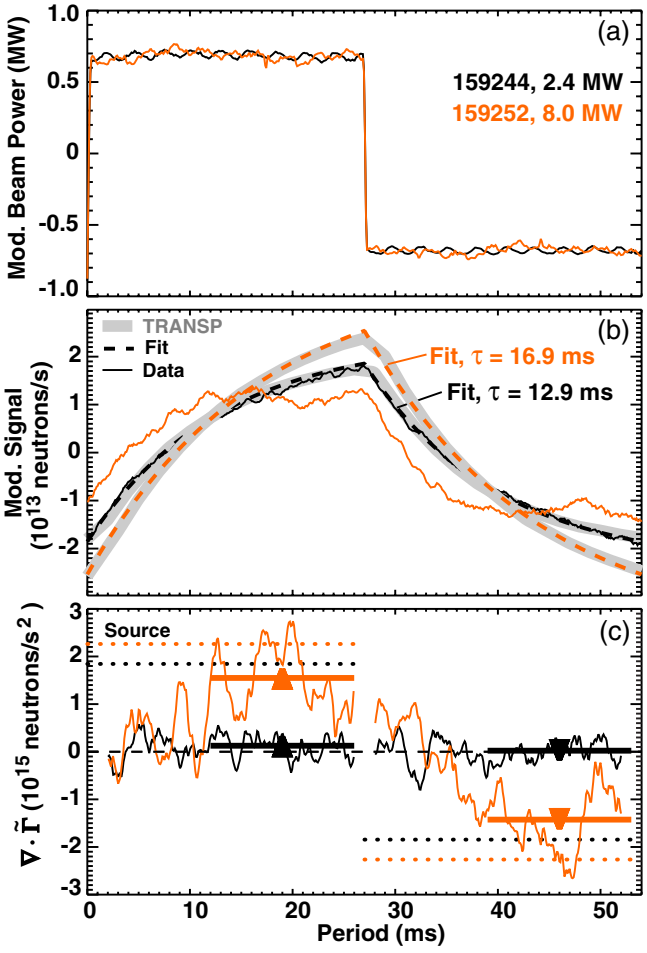

Figure 4. Example transport analysis with conditionally averaged, detrended (*a*) modulated beam power, (*b*) expected and measured neutron rate waveforms, and (*c*) calculated transport for two different beam powers.

The analysis assumes the linearized continuity equation to solve for divergence of modulated fast-ion flux,

$$\nabla \cdot \tilde{\Gamma} = -\frac{\partial \tilde{n}}{\partial t} + \tilde{S} - \frac{\tilde{n}}{\tau}. \quad (1)$$

The quantities in equation (1) depend on the multi-dimensional weight function inherent to each diagnostic, as described in section 2. The measured $\tilde{n}$ is the modulated population of fast ions that appears in the volume of phase-space measured by the diagnostic. The diagnostic sensitive region is populated by the modulated neutral beam, $\tilde{S}$, while particles thermalize through a sink term that depends on the diagnostic-weighted slowing down time, τ. The inferred $\nabla \cdot \tilde{\Gamma}$ represents transport of fast ions with a wide range energies; the NPA diagnostic detects deuterium particles with energy greater than 25 keV and is mainly sensitive to energies ranging from 40–80 keV, the neutron signal results from fusion reactions from fast ions with energies in the general range of 50–80 keV and is most sensitive to energies greater than 70 keV, and the FIDA signal is found by integrating over the line-of-sight energy range of 21–61.3 keV. In the absence of AE-induced transport, the left hand side of this equation is assumed to be zero.

The quantities $\tilde{S}$ and τ are found from fits of the expected signals for the single modulated neutral beam source calculated by the NUBEAM module of TRANSP assuming classical transport (no anomalous diffusion). The evolution of the perturbed response depends on plasma parameters, so $\tilde{S}$ and τ must be calculated for each shot and each time range used for conditional averaging. The expected neutron signals are calculated directly by TRANSP. Further processing of TRANSP results is done by the forward modeling code FIDASIM to apply the weight function and produce the expected signals for the NPA and FIDA diagnostics. The expected signals are then analyzed over the same energy range and conditionally averaged in the same manner as the data. Figure 4(*b*) shows the expected neutron signal, and the dashed line is the fit of the expected signal using equation (1) with $\nabla \cdot \tilde{\Gamma} = 0$ using the marked values of τ and $\tilde{S}$.

The data signals are absolutely calibrated by matching the raw signals to the expected TRANSP/FIDASIM signals for the lowest power shot on the day of the experiment. Using the measured $\tilde{n}$, the quantity $\nabla \cdot \tilde{\Gamma}$ is determined by equation (1) and plotted in figure 4(*c*). In the high power case, $\tilde{n}$ differs substantially from the expected signal (orange line in figure 4(*b*)), which corresponds to a larger value of $\nabla \cdot \tilde{\Gamma}$. The $\nabla \cdot \tilde{\Gamma}$ evolves in time as fast-ions diffuse in space and energy through the diagnostic-sensitive region, so transport is quantified by taking a time-average in the first (upward triangles) or second (downward triangles) half-period. The time-average is taken over the latter 14 ms of each half period for the neutron and FIDA diagnostics, and the latter 16 ms of each half period for the NPA diagnostic. Note that in this formulation, a positive (negative) value of $\nabla \cdot \tilde{\Gamma}$ in the first (second) half period means that transport causes a net flow of particles out of the part of phase space measured by the diagnostic.

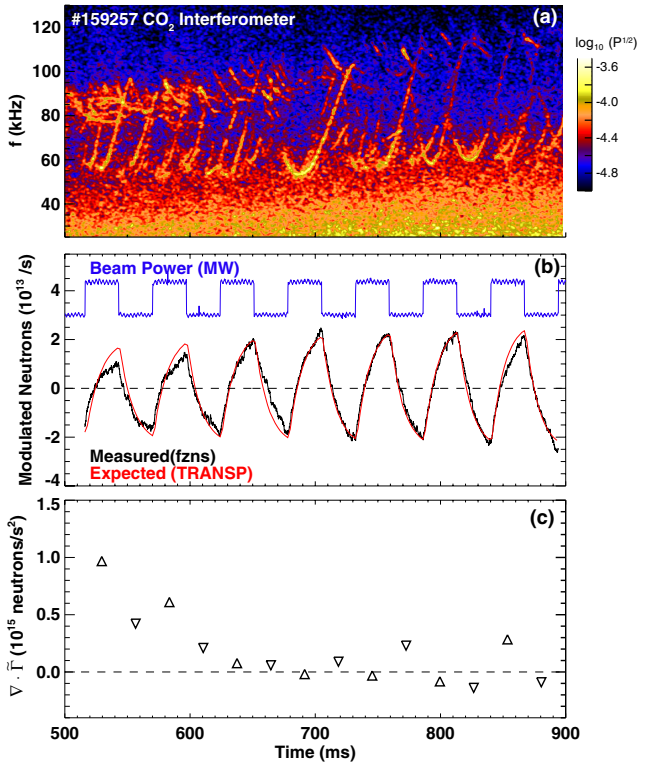

Figure 5. Transport behavior near threshold, measured by the neutron diagnostic. In (*a*), density fluctuations show TAE and RSAE activity early in the shot, with mainly RSAE activity later in time. In (*b*), the detrended neutron signal is compared to the expected signal from TRANSP, and (*c*) shows the inferred fast-ion transport decreases in time as the signals become classical.

4. Threshold behavior of AE transport

The threshold behavior of $\nabla \cdot \tilde{\Gamma}$ can be seen by analyzing the time dependence of fast-ion diagnostic density during the current ramp. In figure 5(*a*), frequency sweeping RSAEs and near-constant frequency TAEs are observed in cross-power density fluctuation spectra from CO_2 interferometer chords in a relatively low power, 'near-threshold' shot. Figure 5(*b*) shows that the amplitude of modulation in the measured neutron signal is smaller than expected early in the discharge. In figure 5(*c*), the calculated transport is large early in the discharge and drops to immeasurable levels, even though AE modes are still present later in the discharge.

This threshold observation is shown in terms of the conventional critical gradient paradigm in figure 6. In figure 6(*a*), the classical beam density profile was calculated by TRANSP using the neutral beams, plasma profiles, and MSE constrained EFITS from the experiment, and the peak in the radial beam density gradient (which occurs near the normalized minor radius $\rho_N \sim 0.37$ in this case) is plotted versus time. The profile flattens in time, and the modulated beam acts to incrementally increase the radial gradient. In figure 6(*b*), for each modulation period, the average measured incremental transport (i.e. the average of the 'up' and 'down' triangles at each period in figure 5(*c*)) is plotted versus the average classical

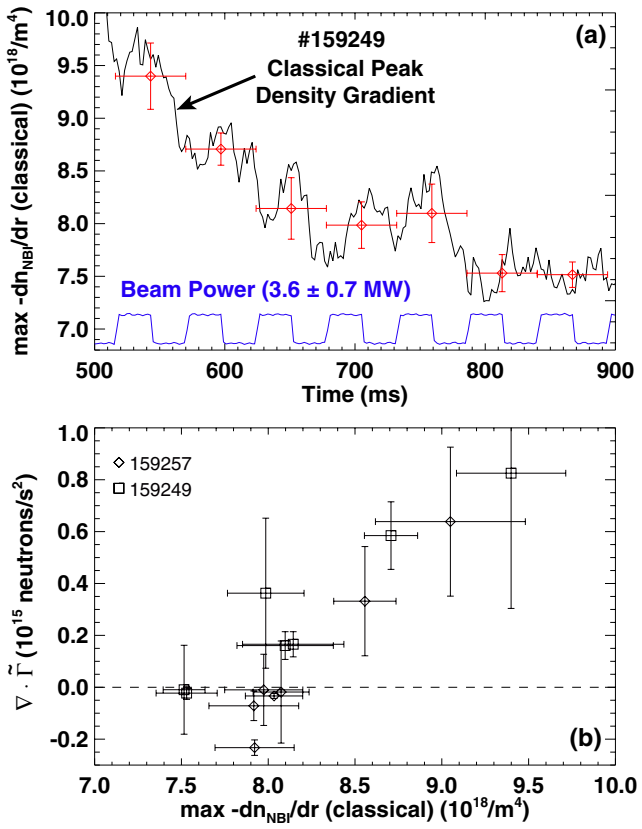

Figure 6. Measurements of incremental transport are used to empirically find the critical beam density gradient for specific experiment conditions. In (*a*), the classical peak beam density gradient predicted by TRANSP is plotted versus time, where red diamonds indicate the average over the beam period. In (*b*), the measured transport inferred from the neutron diagnostic versus average classical peak beam density gradient is plotted for each period. The critical gradient threshold is near 8×10^{18} m^{-4}.

peak beam density gradient (red diamonds in figure 6(*a*)) for two duplicate shots. When the gradient exceeds 8×10^{18} m^{-4}, AE's cause a sudden increase in fast-ion transport. According to critical gradient theory, the particles are consequently redistributed (radially in most models, although redistribution can occur in both position and velocity space) so that the driving gradient relaxes to the critical value and AEs maintain marginal stability.

The phase-space dependence of AE transport can be seen in figure 7. Each data point is the average of $\langle \nabla \cdot \tilde{\Gamma} \rangle$ from the first and second half periods after conditionally averaging several periods in each shot. Beam power scans using purely tangential sources, purely perpendicular sources, and mixed sources are compared. The measured transport threshold varies between fast-ion diagnostics that are sensitive to different regions in phase space. In figure 7, the $R = 1.8$ m NPA chord and the $R = 2.1$ m FIDA chord measure a rise in transport above ~4 MW beam power, while the neutron diagnostic measures the onset of transport at a much lower beam power. Figure 7(*d*) shows the amplitude of modulated fast ion losses begin to grow above 3 MW. Note that the mixed beam, tangential, and perpendicular beam power scans took place on different days. The NPA, neutron, and FIDA diagnostics have been absolutely calibrated for comparison, but the FILD diagnostic is not calibrated. However, the FILD settings for the tangential and perpendicular scans were similar. Interestingly, the lower FILD detector detects more losses of modulated beam particles in the perpendicular beam power scan compared to the tangential beam power scan.

A convenient quantity often used in evaluating fast-ion performance is the ratio of total measured neutron rate to the predicted rate calculated by the TRANSP NUBEAM code [3] assuming no anomalous transport. In the presence of AEs, the ratio of the measured neutron rate to the predicted rate is often below one. Figure 8 shows transport versus the signal-to-classical ratio for each shot in the power scan, where transport is time-averaged over several periods for the first (upward triangles) or second (downward triangles) half-period. For the neutron diagnostic, which is broadly sensitive to the higher energy ions, the incremental transport increases when the signal-to-classical ratio drops below 0.9. On the other hand, the neutral particle analyzer, which has narrow sensitivity to the trapped portion of 40–80 keV ions, measures a jump in incremental transport below a ratio of approximately 0.7.

The stiffness of the inferred transport changes as beam deposition shifts AE induced transport to different regions of phase space. As shown in figure 2, for a given beam power, tangential beam injection results in stronger total AE amplitude compared to perpendicular beam injection. However, figure 7(*a*) shows that the measured transport is more or less the same at each beam power. When the measured transport is plotted versus AE amplitude (figure 9), the apparent conclusion is that perpendicular beam injection is more efficient at generating wave-particle resonances for trapped particles, so greater transport is measured by the NPA. However, further theoretical analysis presented in section 5 shows that the fundamental linearity assumption of equation (1) is violated because the modulated beam modulates the AE amplitude. It will be shown that a more careful transport analysis technique that includes a time-varying source is required to fully quantify stiffness.

4.1. Effects of ECH on fast-ion transport

Transport properties were also observed to change when the types of AEs were altered using ECH. Recent studies have shown that RSAEs can be suppressed by using ECH to locally increase the electron temperature near $q_{\min}$, which modifies the AE continuum to the point that typical frequency-sweeping RSAEs are no longer eigenmodes of the system [31]. Figure 10(*a*) shows an example spectrogram of density fluctuations from the tangential beam power scan, where a mix of RSAEs and TAEs were excited. When the same shot was repeated with ECH near $q_{\min}$, the rapidly chirping RSAEs were absent, and the spectrum featured more slowly evolving, TAE-like modes (figure 10(*b*)). In figures 10(*c*) and (*d*), the background-subtracted FIDA density profiles, measured later in the current ramp at $t = 1030$ ms, are plotted for various NBI powers. We find that higher fast-ion densities were reached with ECH. This is likely due to a combination of effects. First,

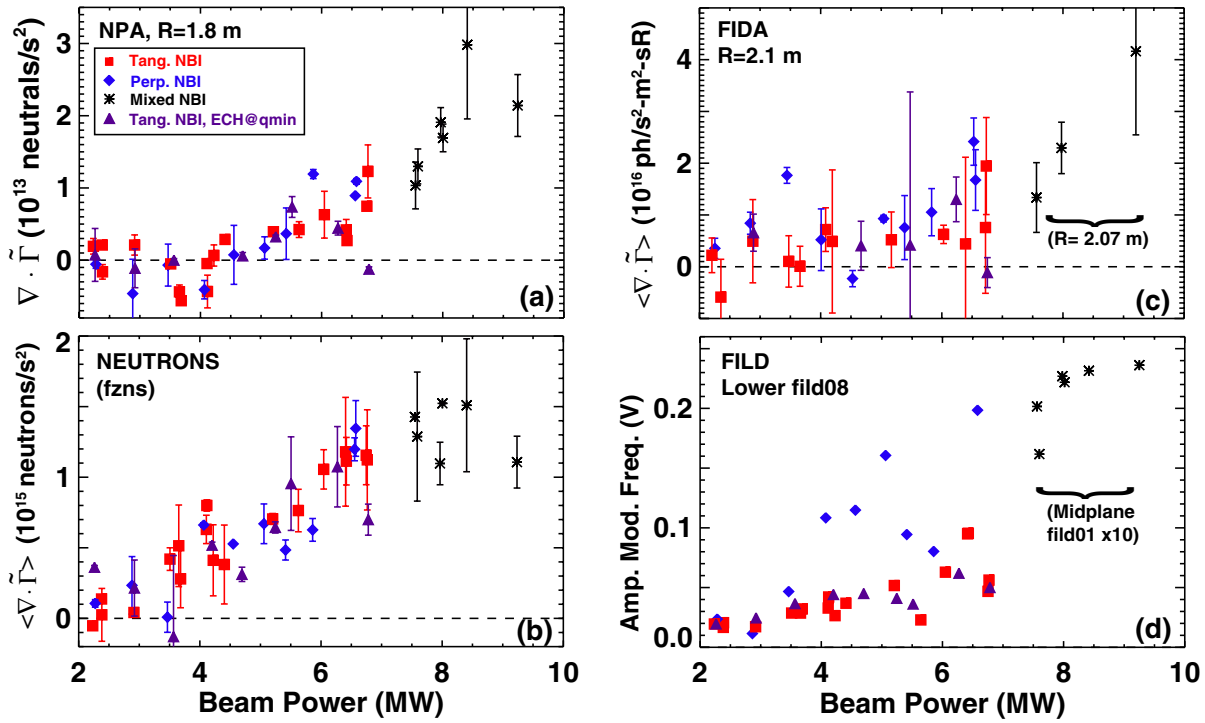

Figure 7. Time-averaged divergence of modulated flux (transport) versus total beam power for (*a*) NPA, (*b*) neutron, (*c*) FIDA diagnostics. In (*d*), the amplitude of the modulated beam particle losses recorded by the midplane and lower FILD detectors is plotted versus beam power.

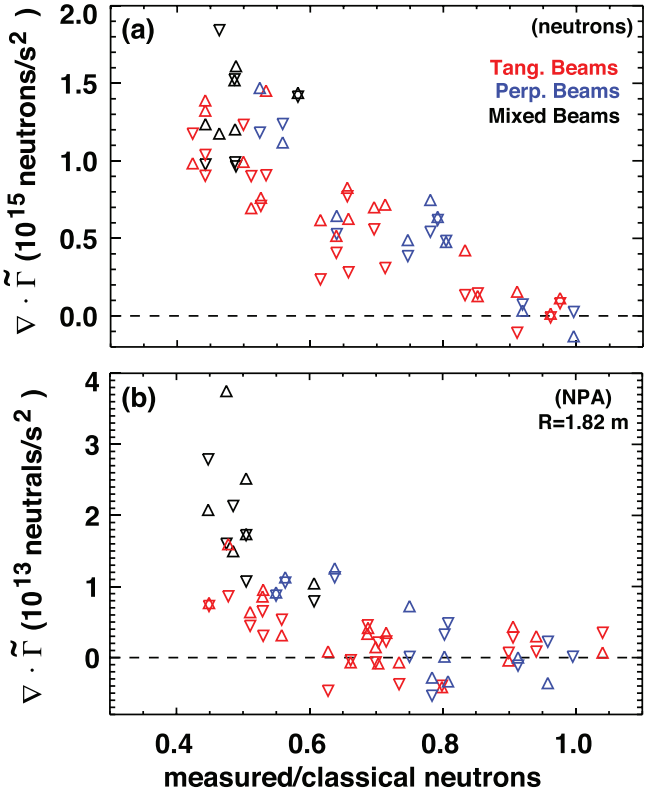

Figure 8. Transport inferred from the (*a*) neutron diagnostic and (*b*) NPA diagnostic versus the ratio of the measured to expected neutron rates. The difference in the onset of transport between the two diagnostics indicates that transport is a phase-space dependent quantity.

ECH reduces fast ion transport by reducing the total mode activity (reduction of mode activity with ECH is also evident in figure 2(*f*)). Second, the electron heating increases

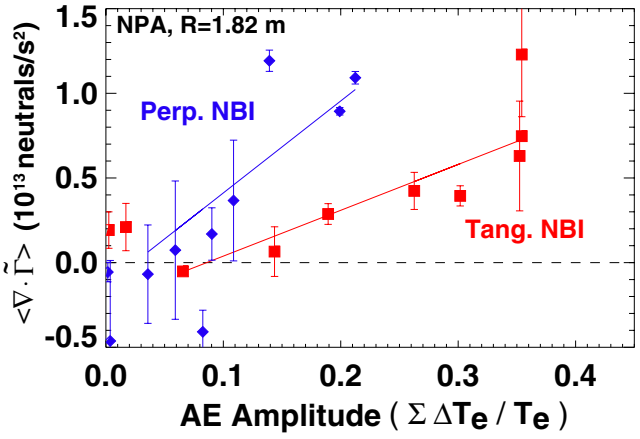

Figure 9. Transport inferred from the NPA diagnostic versus AE amplitude indicates that perpendicular beam injection is more efficient at driving modes that transport trapped particles compared to tangential beam injection.

the fast-ion slowing down time (figures 10(*e*) and (*f*)), which decreases collision frequency and builds the confined fast ion density. Thus, we see that there is an empirical critical gradient for a given condition (figure 6) which was altered when ECH suppressed RSAE activity (figures 10(*c*) and (*d*)).

5. Fast ion transport modeling

Theoretical analysis previously presented in [25] shows that the measured onset threshold for fast-ion transport corresponds to the threshold in the number of fast-ion orbits that become stochastic after interaction with AEs. In this section, we present details of the theoretical 'stochasticity analysis'

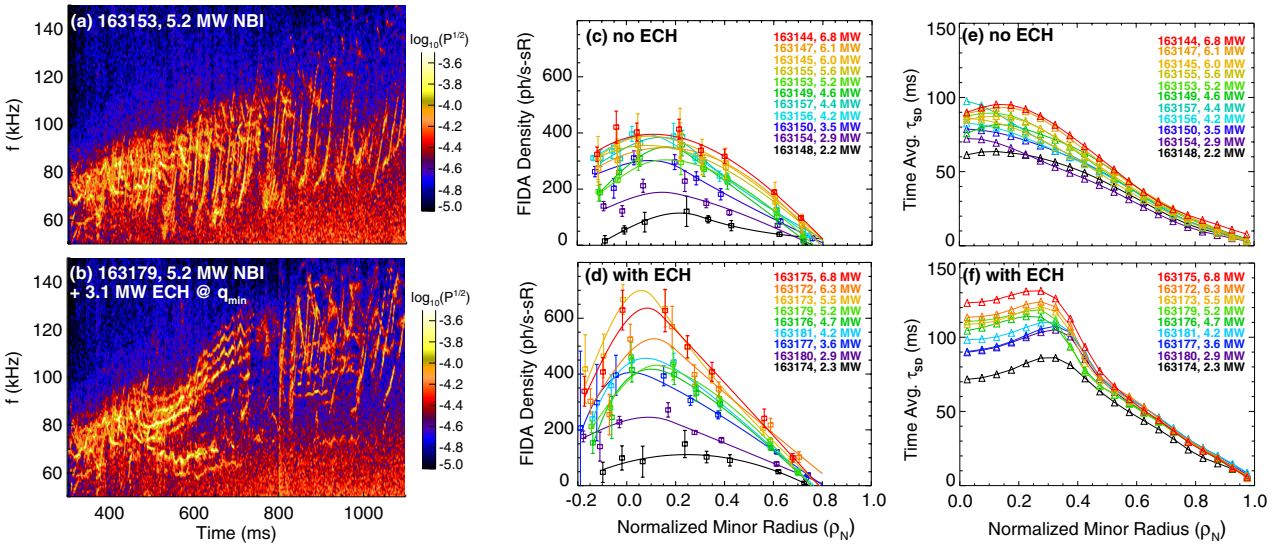

Figure 10. ECH near $q_{\min}$ beginning at $t = 450$ ms results in TAE dominant mode spectrum and increased FIDA density. Comparison of CO_2 interferometer spectrogram at 5.2 MW NBI (*a*) without ECH and (*b*) with 3.1 MW ECH. FIDA density profiles measured at $t = 1030$ ms for various NBI powers (*c*) without ECH and (*d*) with ECH. The FIDA density was found by dividing the FIDA brightness by the injected neutral beam pencil density. The classical slowing down profile calculated by TRANSP is time-averaged between $t = 500$–750 ms for all of the beam powers in the tangential beam power scan (*e*) without ECH and (*f*) with ECH.

used in reference [25] and apply the analysis to a second case. We confirm that the threshold found with the stochasticity analysis is again in good agreement with the data. In section 4, similar levels of above-threshold transport were measured with either tangential or perpendicular beam injection for a given total beam power. In this section, we find that the stochasticity analysis does not reproduce the relative measured levels of transport, or stiffness. Further investigation using a time dependent transport model shows that the interpretation of the measured transport is significantly complicated by the nonlinear effect of modulated AE amplitude. Quantification of stiffness using measurements from critical gradient experiments with beam modulation will require careful treatment and is reserved for future publications.

5.1. Stochasticity analysis using ORBIT

To begin, we examine the interaction of AEs in fast-ion phase space using NOVA and the guiding center code ORBIT. Using a well-established method [37], the AE mode structures are first calculated with the ideal MHD eigenvalue solver NOVA [38] with the fitted plasma profiles and kinetic equilibrium reconstruction as input. NOVA finds all possible eigenmodes (including radial harmonics) for a given toroidal mode number in a given frequency range. In order to discriminate which solutions are experimentally observed, NOVA eigenmode solutions are compared to experimental data using magnetics to determine toroidal mode number and ECE temperature fluctuation to compare radial mode structures. The matching radial mode structures are then scaled in amplitude to match the coherent AE-induced ECE temperature fluctuation measurements. An example of a scaled $n = 4$ RSAE is shown in figure 11. Often, the radial mode structures calculated by NOVA must be shifted radially, sometimes up to 7 cm, in order to match the ECE $\tilde{T}_e$.

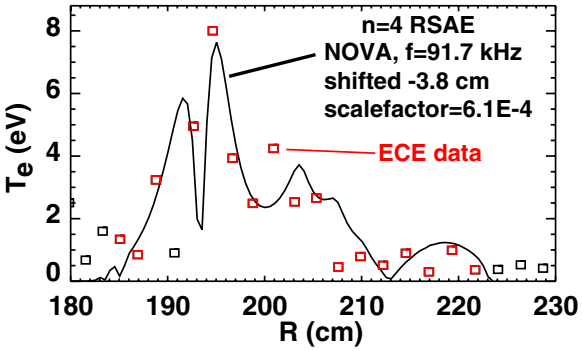

Figure 11. Example of the scaling of an $n = 4$ RSAE radial temperature fluctuation calculated by NOVA (solid black line) to the ECE $\tilde{T}_e$ measurements that have greater than 80% coherence (red squares). The NOVA mode is shifted inward radially and scaled in amplitude through least squares fitting. The amplitude scaling is used to find the final scaling factors listed in tables A1 and A2.

The NOVA radial mode structures are also often more narrow in radius compared to the ECE measurements, and the NOVA mode frequencies can differ by up to 15% from the measured frequencies, especially for rapidly chirping RSAE modes. Differences between the calculated NOVA modes and the measurements are attributed to uncertainty in the kinetic equilibrium reconstructions. Nonetheless, the results presented in this paper show that the analysis is relatively insensitive to these differences, so the radial mode structures calculated by NOVA appear adequate.

Next, the set of scaled AE eigenfunctions from NOVA, along with the background equilibrium field, are used as input to ORBIT. Following the procedure similar to the one in reference [39], ORBIT tracks the fast ion trajectories to determine which orbits have good Kolmogorov–Arnold–Moser (KAM) surfaces and which orbits become stochastic [40] due to AEs. Particles are typically followed for 15–20 toroidal transit

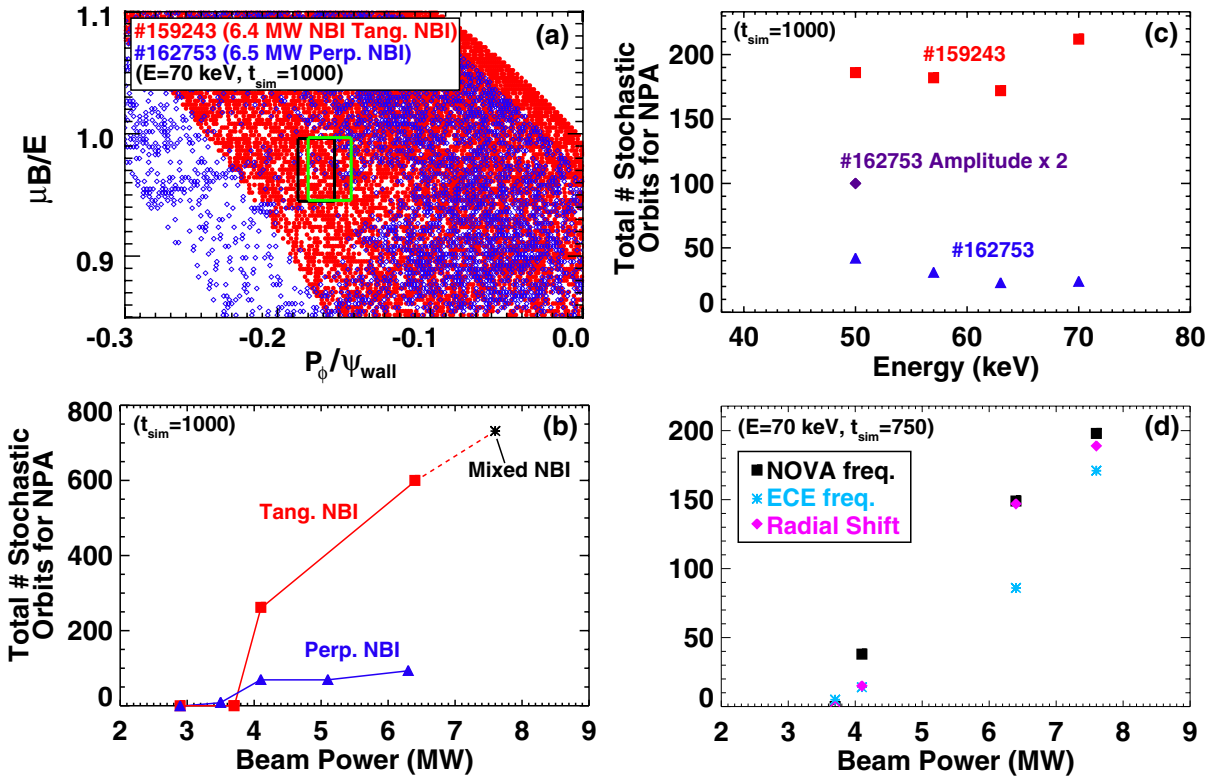

Figure 12. Theoretical stochasticity analysis. (*a*) ORBIT analysis of two discharges using different beam geometries at nearly identical total beam power for 70 keV particles, where a dot is drawn when orbits become stochastic after 20 transit times (~4μs per transit time). The NPA diagnostic region is identified by the green box for #159243 and black box for #162753. (*b*) The sum of the stochastic orbits in the NPA region for particles with $E = 50$, 57, 63, 70 keV is plotted versus beam power. (*c*) The total number of stochastic orbits in the NPA region versus particle energies for #159243 (red square), #162753 (blue triangle), and for #162753 with doubled mode amplitudes (purple diamond). (*d*) Sensitivity study on how the total number of stochastic orbits versus beam power depends on mode frequencies calculated by NOVA (black square), actual frequencies measured by ECE (blue asterisk), and radially shifting the NOVA modes to better match the measurements (pink diamond).

times, or 60–80 μs, and the simulations do not include collisions. The results of the stochasticity analysis are presented in figure 12.

The stochasticity analysis indicates that, for a given total NBI power, tangential NBI results in greater stochasticity of trapped particle orbits compared to perpendicular NBI. This is in contrast with the measurements in figure 7, where similar levels of above-threshold transport were measured with either tangential or perpendicular NBI. In figure 12(*a*), we plot the orbits for $E = 70$ keV particles that become stochastic in orbit topology space near the NPA diagnostic region of phase space and compare two shots with different beam injection geometries. Both shots had similar total beam power and are analyzed at a similar timeslices near $t = 790$ ms, when $q_{\min} \sim 3$. A list of the modes and amplitude scaling factors used by ORBIT for each shot can be found in the appendix. The tangential NBI shot #159243 used the scaled NOVA eigenmode frequencies and structures for 8 RSAEs and 3 TAEs, resulting in many stochastic orbits in the NPA diagnostic region of phase space (red dots inside of green box). The perpendicular NBI case #162753 had comparatively fewer modes with 5 RSAEs and 3 TAEs, which resulted in a fewer number of stochastic orbits (blue dots inside of black box) compared to the tangential NBI case #159243.

The stochasticity analysis shows that the onset threshold for stochastic orbits occurs near 3.7 MW beam power regardless of beam injection geometry, consistent with the experimental threshold measurements in figure 7. In figure 12(*b*), the sum of the stochastic orbits in the NPA region for particles with $E = 50$, 57, 63, 70 keV is plotted versus beam power. Rather than repeating the time-intensive full analysis for each shot in the power scan, the NOVA eigenmodes from #159243 (#162753) were rescaled to match the measured ECE radial mode structures observed in shots at different beam powers from the tangential (perpendicular) NBI power scan. In general, the mode structures are similar between shots, and both the total number of modes and the mode amplitudes decrease with beam power.

It is important to note that the stochasticity analysis presented here applies to a single timeslice, while the experimental transport measurements are generally analyzed over several hundred millisecond time periods, during which the AE mode activity evolves. In particular, RSAEs sweep in frequency and shift radially with $\rho_{q\min}$. Therefore, a sensitivity study was conducted in order to gauge how much the stochasticity analysis for the NPA diagnostic is affected by particle energy, mode amplitude, frequency, and radial position. Figure 12(*c*) shows the total number of stochastic orbits in the NPA region versus energy for shots #159243 and #162753. We find that for this diagnostic,

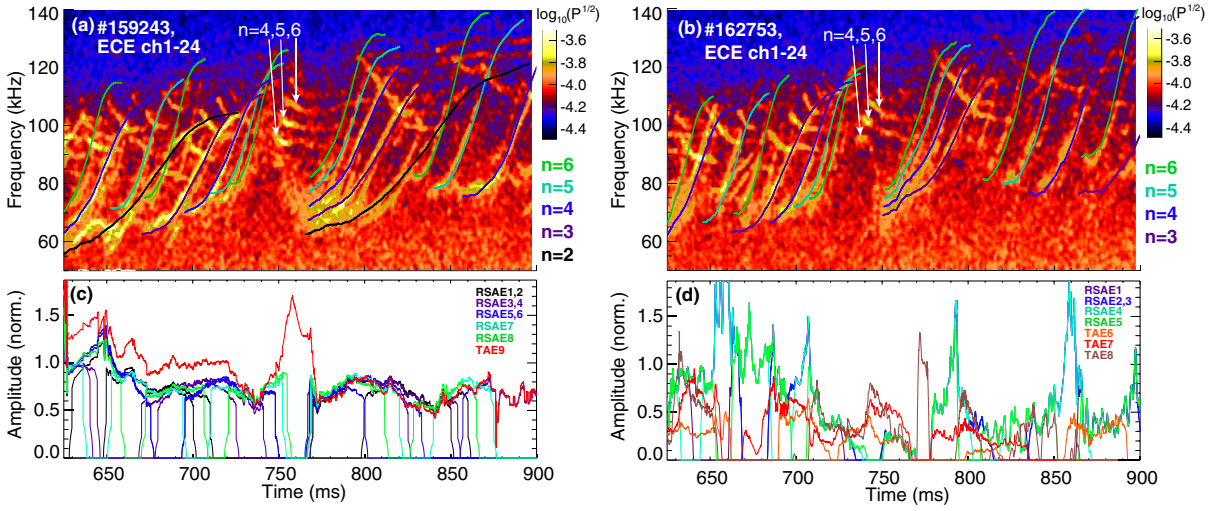

Figure 13. (*a*) and (*b*) ECE power spectrum with an overlay of the modes used in the kick model. NOVA modes were scaled to experiment around $t \sim 800$ ms for #159243 and $t \sim 790$ ms for #162753. The ad hoc RSAE model [31] is used, along with magnetics, to confirm toroidal mode numbers. (*c*) Time evolution of amplitudes determined from the kick model for #159243 and (*d*) #162753.

stochastic orbits have a weak dependence on particle energy, but strong scaling with mode amplitude. In figure 12(*d*), ORBIT was re-run for the tangential beam power scan using the measured ECE frequencies listed in table A1. Since the position of $q_{\min}$ changes with total beam power, ORBIT was also re-run with all modes shifted radially by $\Delta\rho = [-.097, -.044, 0, +.056]$ for $P_{\mathrm{NBI}} = [3.7, 4.1, 6.4, 7.6]$ MW. In all cases, the onset of stochastic orbits near 4 MW is consistent with the measured NPA transport threshold in figure 7(*a*).

5.2. Kick model analysis

Results show that the single-timeslice stochastic analysis is fairly robust for determining the onset of transport, but understanding the absolute scaling of transport requires further investigation. As a next step, we calculate the time-evolved transported fast-ion distribution function using the kick model [41]. This reduced model is implemented within the NUBEAM module of TRANSP and uses the ORBIT code to calculate the probability matrix for particle steps in phase space resulting from resonant wave-particle interactions with AEs. In this study, multi-timeslice, monotonically evolving kinetic equilibrium fits were generated using OMFIT [42] and an analytic fit of the measured AE mode spectrum to determine the evolution of $q_{\min}$ (as described in section 2). The experimental plasma profiles and kinetic EFITs were used as input to a classical TRANSP run to define the initial conditions for the kick model, and the same TRANSP run was used as input to the NOVA code to generate AE mode structures. Figures 13(*a*) and (*b*) show the time evolution of the fitted AE modes overlayed with the ECE spectrogram for shots #159243 and #162753. The kick model analysis grouped RSAEs with the same toroidal mode numbers together, and all TAEs were grouped together. The AE mode amplitudes were scaled to match the ECE data at timeslices near the RSAE cascade when $q_{\min} \sim 3$. The model then scales the amplitudes of the modes in time (figures 13(*c*) and (*d*)) to match the measured neutron rates.

The initial analysis of shot #159243 was recently reported in [26] and reveals a significant complication: the modulated beam also modulates the AE amplitude, which increases transport of the background source beam particles and strongly influences the shape of the distortion in the waveforms measured by the fast-ion diagnostics. Figure 14 compares conditionally averaged signals from $t = 678$–894 ms for shots #159243 and #162753. In figure 14(*a*), the total AE amplitude measured by ECE grows in the first half period when the beam is on and decays in the second half period when the beam is turned off. In figure 14(*b*), the total simulated mode amplitude evolution from figures 13(*c*–*d*) is conditionally averaged and shows modulation of mode amplitude similar to figure 14(*a*). In both shots, the timing of the beam modulation is identical, however, the modulated AE amplitude grows earlier in #162753 because the current profile evolves slightly faster, e.g. $q_{\min} = 3$ at roughly $t = 764$ ms for #162753 and $t = 778$ ms for #159243. Using the simulated amplitude, the kick model very closely replicates the distorted waveforms of both the neutron and NPA diagnostics (figures 14(*c*) and (*e*)).

The nonlinear effect of AE amplitude modulation is important in understanding transport scaling. In figures 14(*d*) and (*f*), the kick model is re-run with the same mode amplitudes, but with the modulated beam only, showing that in fact the modulated beam particles undergo minimal transport and result in a near-classical signal. When the model is re-run with the background source beams only (no modulated beam), it is found that most of the deviation from the classical diagnostic signal is due to transport of the background beam particles. In figures 14(*d*), the AE amplitude grows earlier in the perpendicular beam case, causing the neutron signal to decay earlier. This phase difference can result in an amplified level of inferred transport relative to the tangential beam injection, since the time-average of the divergence of flux is taken over the same latter portions of the half period. Therefore, it is not straightforward to do a quantitative comparison of the transport stiffness of tangential versus perpendicular NBI because

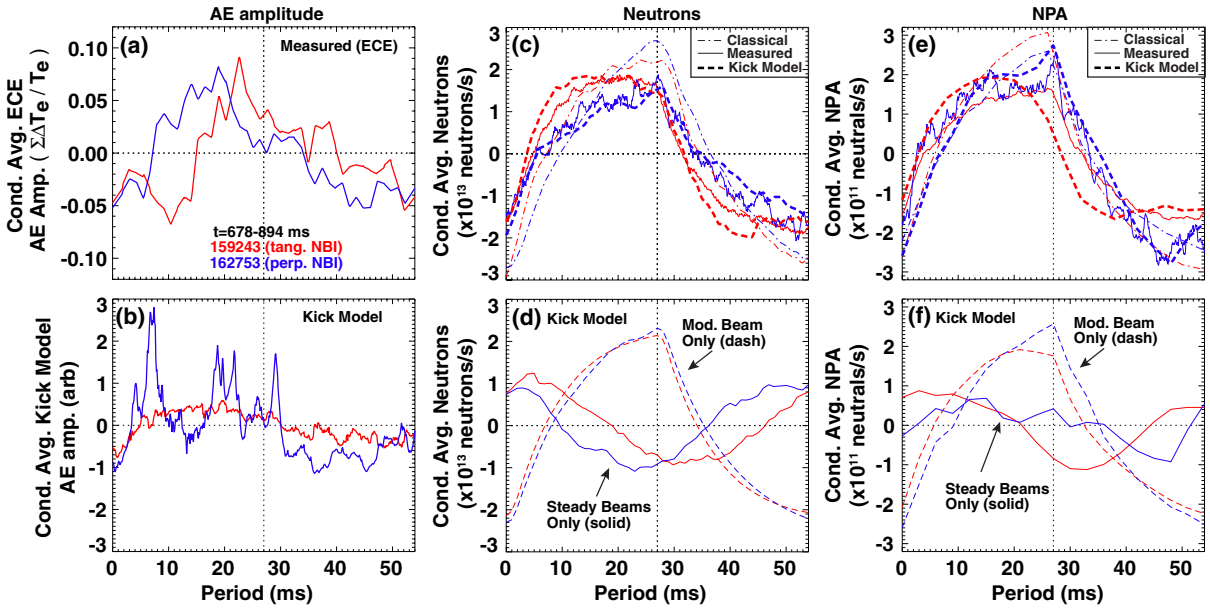

Figure 14. Comparison of conditionally averaged data and modelled signals from $t = 678$–894 ms for shot #159243 (6.4 MW tangential beam injection) in red and shot #162753 (6.5 MW perpendicular beam injection) in blue. AE amplitude modulation is observed in (*a*) ECE data and (*b*) the kick model. Analysis is shown for ((*c*) and (*d*)) neutron and ((*e*) and (*f*)) NPA diagnostics. The neutron data is from 'fzns' with calibration factors $\text{cal}_{159243} = 2.07 \times 10^{15}$ and $\text{cal}_{162753} = 2.58 \times 10^{15}$. The NPA data is from 'ssnpa1' with $\text{cal}_{159243} = 7.11 \times 10^{12}$ and 'ssnpa3' with $\text{cal}_{162753} = 1.64 \times 10^{13}$. In (*c*) and (*e*), the kick model (dashed line) reproduces the measured signal (solid line), which differs from the expected signal from classical TRANSP run (dash-dot line). In (*d*) and (*f*), the kick model is re-run with the same AE amplitudes from figures 13(*c*) and (*d*), either with steady beam injection only, or with modulated beam injection only. The nonlinear modulation of the 'steady' beam fast-ion population significantly contributes to the measurement.

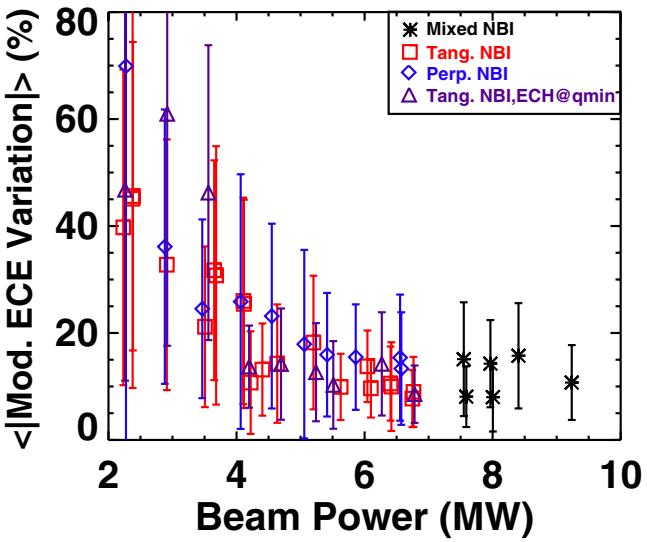

Figure 15. The absolute value of the % variation of the conditionally averaged AE amplitude measured by ECE is time-averaged over the period and plotted versus total injected beam power. The modulated beam causes variation in the measured AE amplitude, with the largest variation in shots with the lowest total beam power.

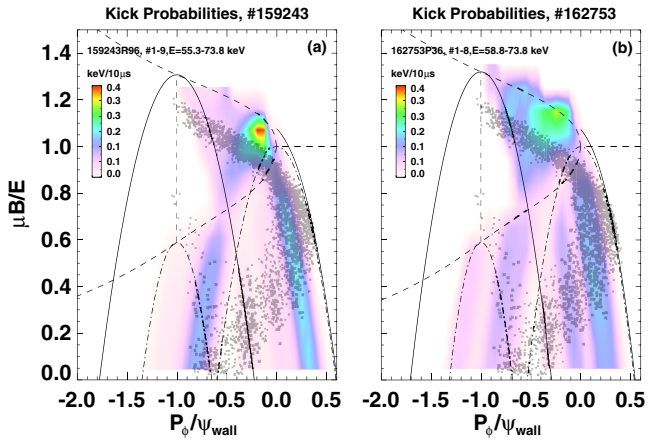

Figure 16. Comparison of average kick probabilities for (*a*) shot #159243 at $t \sim 811$ ms with 6.4 MW tangential beam injection, and (*b*) shot #162753 at $t \sim 790$ ms with 6.5 MW perpendicular beam injection shows that the relative magnitude of the kick energies are similar in the parts of phase space that overlap with the modulated neutral beam (grey dots).

the linear assumption that the source of modulated particles is constant in time (as plotted in figure 4(*c*)) no longer holds.

Even though perpendicular injection generates a smaller number of generally weaker AEs compared to tangential beam injection, the modulated AE amplitude is similar in magnitude. This can be seen in figure 14(*a*), as well as figure 15, where the variation in AE amplitude is plotted versus total beam power for all shots presented in this paper. This is likely because the AE modes overlap with the modulated beam particles in phase space, as shown in figure 16 where the birth population of 70 keV modulated beam particles is overlayed with a colormap of the root-mean-square energy of the kicks from the AEs.

The kick model shows that AE transport leads to significant changes in the neutral beam density and current profiles depending on injection geometry. Figures 17(*a*) and (*b*) show

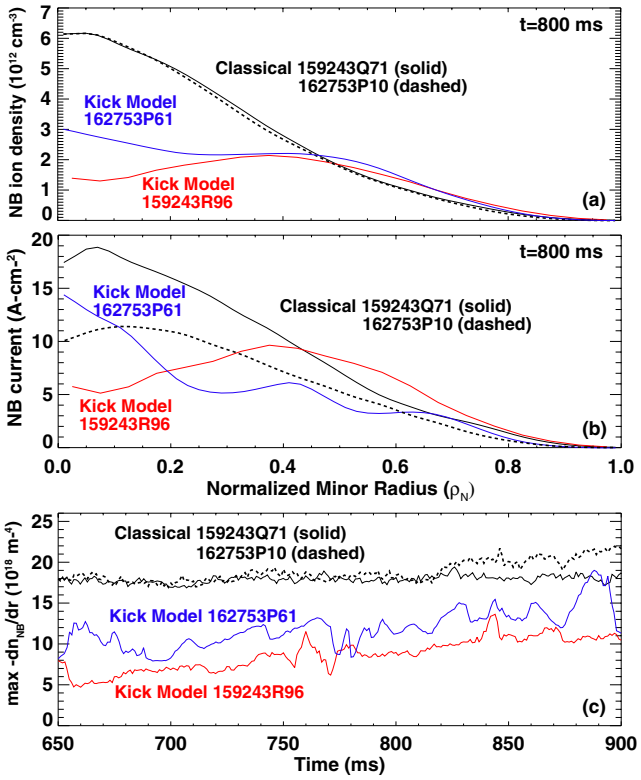

Figure 17. Comparison of kick model (*a*) transported fast ion profiles and (*b*) current profiles for tangential beam injection (red) and perpendicular beam injection (blue) at at $t = 800$ ms. (*c*) Time history of peak beam density gradient from the kick model.

comparisons of the beam density and current profiles predicted by the kick model for both tangential (red) and perpendicular (blue) injection. In both cases, the fast ion density profile flattens, the core density drops by 50% or more, and density exceeds the classical expected values at large radii. In the tangential beam case, transport by AEs leads to hollow beam density and current profiles. In [26], the kick model fast ion distribution function for #159243 was further processed with the FIDASIM code to produce FIDA signals. Excellent agreement was found, and the hollow beam density profile was confirmed by the fast ion profiles measured by the FIDA diagnostic. While RSAEs are destabilized near $\rho_{\rm qmin}$, the observed modes have relatively broad structure (see for example, figure 11). Since typical 75 keV fast-ion orbits are large and pass through both the magnetic axis and $\rho_{\rm qmin}$ (as illustrated in figure 8 of [26]), RSAEs in particular could drive substantial outward transport at small ρ, creating hollow beam density profiles. In the perpendicular beam injection case, there are fewer RSAEs, and the kick model shows that the AE transport results in relaxed, but not hollow fast-ion density profiles (blue line in figure 17(*a*)). In both cases, it is found that the AE transport results in mainly redistribution, not loss, of non-inductive current drive. These results show that treatment of the AEs in phase space is important in accurately predicting fast ion density and current profiles, highlighting the importance of including the velocity dependence of the fast-ion distribution function in critical gradient models which are currently commencing [43].

The critical peak beam density gradient calculated from the kick model is in good agreement with the empirical value. Classically, the peak in the density gradient occurs around $\rho = 0.36$ for these cases. Figure 17(*c*) shows the time history of the peak beam density gradient between $\rho \sim 0.25$–0.75 of the transported profiles for above threshold, tangential beam (red) and perpendicular beam (blue) cases. The kick model peak gradient values near $t = 700$ ms are around 8×10^{18} m^{-4}, in good agreement with the measurement in figure 6. The kick model critical (radial) gradient increases with a $1/q_{\rm min}^2$ dependence as the discharge evolves, roughly doubling between $q_{\rm min} \sim 3.4$ at $t = 650$ ms and $q_{\rm min} \sim 2.5$ at $t = 900$ ms.

6. Summary

Experiments in the DIII-D tokamak show that many overlapping, small-amplitude Alfvén eigenmodes cause stiff fast-ion transport above a critical threshold. AE transport is inherently a phase-space dependent quantity, and the measured threshold varies between fast-ion diagnostics because each diagnostic measures a different part of phase space. Both experimental measurements (figure 5) and theoretical analysis using the ORBIT code (figure 12) clearly indicate that the stiff transport threshold exceeds the linear threshold for AE stability. In other words, some AEs can be tolerated before significant fast-ion transport occurs. The sudden rise in measured transport corresponds with the onset of orbit stochasticity that occurs when multiple AEs create wave-particle resonances that overlap in phase space.

The effects of altering the fast ion distribution function with different beam injection geometry was studied in detail. No significant differences in the onset threshold outside of measurement uncertainties were found, in good agreement with the theoretical stochastic threshold analysis for the NPA diagnostic. However, a direct relation between the number of stochastic orbits in the diagnostic part of phase space and the measured fast-ion flux has not been validated. In the experiment, perpendicular beam injection results in less total AE mode activity compared to tangential beam injection for a given beam power. While the total theoretical stochasticity is reduced in the perpendicular NBI case, the measured transport was unchanged. Further investigation with the kick model shows that, above threshold, the majority of the response in the data signals is due to modulation of the AE amplitude. Therefore, proper quantification of net fast-ion flux will require inclusion of this nonlinearity. The kick model has emerged as a powerful tool for accurately calculating the time evolution of AE induced transport and understanding the measured signals. While the model evolves the AE amplitude based on previously measured magnetics or neutron rate, it could be generalized to do predictive studies by implementing a critical gradient model to calculate a physics-based, phase-space dependent diffusion coefficient.

Finally, electron cyclotron heating was used to change the mode activity from mixed RSAE and TAEs to a TAE-dominant spectrum. This resulted in higher peak fast-ion densities, suggesting that active control to manipulate AE mode activity can be used, for example, to alter the radial fast-ion critical gradient. The results of this work are being

Table A1. List of mode amplitude scaling factors used in the ORBIT stochasticity analysis for cases with different total tangential beam injection power. Modes were found for #159243 using NOVA at $t = 790$ ms, and amplitude scale factor for each mode was found by a least-squares fit of the NOVA $\tilde{T}_e$ mode structures to experimental measurements. The same modes from #159243 were then scaled to match similar modes in shots at different beam powers. Scaling factor values are normalized ($\times 10^4$) and are proportional to mode amplitude.

Mode	Toroidal mode number	#159243 NOVA Frequency (kHz)	#159243 ECE Frequency (kHz)	#159244 2.9 MW amplitude	#159257 3.7 MW amplitude	#159248 4.1 MW amplitude	#159243 6.4 MW amplitude	#159256 7.6 MW amplitude
RSAE	2	68.1	63.0	0	3.5	1.9	2.2	2.5
RSAE	2	75.2	67.9	0	0	0	4.6	6.4
RSAE	3	80.1	69.3	0	0	11.2	4.8	0
RSAE	3	86.1	75.2	0	6.3	5.1	7.0	3.3
RSAE	4	91.7	79.1	0	0	0	6.1	0
RSAE	4	97.4	85.4	0	5.6	5.7	5.4	5.7
RSAE	5	107.6	98.1	0	0	0	6.6	10.9
RSAE	6	112.2	110.4	0	0	0	7.1	15.5
TAE	5	96.9	101.1	0	0	2.8	2.8	6.1
TAE	6	101.3	107.4	0	0	0	5.4	5.4
TAE	7	105.5	113.3	0	0	0	3.2	3.2

Table A2. List of mode amplitude scaling factors used in the ORBIT stochasticity analysis for cases with different total perpendicular beam injection power. Modes were found for #162753 using NOVA at $t \sim 790$ ms, and amplitude scale factor for each mode was found by a least-squares fit of the NOVA $\tilde{T}_e$ mode structures to experimental measurements. The same modes from #162753 were then scaled to match similar modes in shots at lower beam powers. Scaling factor values are normalized ($\times 10^4$) and are proportional to mode amplitude.

Mode	Toroidal mode number	#162753 NOVA Frequency (kHz)	#162749 2.9 MW amplitude	#162747 3.5 MW amplitude	#162751 4.1 MW amplitude	#162748 5.1 MW amplitude	#162753 6.3 MW amplitude
RSAE	3	65.5	2.7	5.8	6.5	5.3	4.7
RSAE	4	64.0	0	0	0	5.4	3.6
RSAE	4	68.6	0	5.5	6.8	7.0	7.1
RSAE	5	70.4	0	0	0	5.9	5.5
RSAE	6	74.4	0	0	0	0	12.6
TAE	4	77.9	0	0	0	0	6.1
TAE	5	83.9	0	0	8.4	6.9	13.6
TAE	6	88.2	0	0	0	10.1	15.9

applied to guide the development of the Advanced Tokamak scenario to high β_N in DIII-D through the use of tools such as upgraded off-axis neutral beam current drive, electron cyclotron heating [31], and variable beam voltage to alter AE behavior [44] to develop profiles and parameters that are more robust to fast ion redistribution. A key next step for reduced models is implementation for routine analysis and validation of present day discharges in order to better understand how to design optimal scenarios that avoid driving the worst-offending AEs and to give confidence as these models are applied to ITER.

Acknowledgments

This material is based upon work supported by the U.S. Department of Energy, Office of Science, Office of Fusion Energy Sciences, using the DIII-D National Fusion Facility, a DOE Office of Science user facility, under Awards DE-FC02-04ER54698, DE-FG03-94ER54271, and DE-AC02-09CH11466. DIII-D data shown in this paper can be obtained in digital format by following the links at https://fusion.gat.com/global/D3D_DMP.

Appendix. Mode amplitude scaling

References

[1] Heidbrink W.W. 2008 Basic physics of Alfvén instabilities driven by energetic particles in toroidally confined plasmas *Phys. Plasmas* **15** 055501
[2] Gorelenkov N.N. *et al* 2014 Energetic particle physics in fusion research in preparation for burning plasma experiments *Nucl. Fusion* **54** 125001
[3] Pankin A. *et al* 2004 The tokamak Monte Carlo fast ion module NUBEAM in the national transport code collaboration library *Comput. Phys. Commun.* **159** 157
[4] Holcomb C.T. *et al* 2015 Fast-ion transport in qmin > 2, high-β steady-state scenarios on DIII-D *Phys. Plasmas* **22** 055904
[5] Heidbrink W.W. *et al* 2014 Confinement degradation by Alfvén-eigenmode induced fast-ion transport in steady-state scenario discharges *Plasma Phys. Control. Fusion* **56** 095030
[6] Sigmar D.J. *et al* 1992 Alpha-particle losses from toroidicity-induced Alfvén eigenmodes. Part II: Monte Carlo simulations and anomalous alpha-loss processes *Phys. Fluids* B **4** 1506

[7] Berk H.L. *et al* 1995 Line broadened quasi-linear burst model *Nucl. Fusion* **35** 1661
[8] Schneller M. *et al* 2012 Double-resonant fast particle-wave interaction *Nucl. Fusion* **52** 103019
[9] Duong H.H. *et al* 1993 Loss of energetic beam ions during TAE instabilities *Nucl. Fusion* **33** 749
[10] White R.B. *et al* 1995 Toroidal Alfvén eigenmode-induced ripple trapping *Phys. Plasmas* **2** 2871
[11] Darrow D.S. *et al* 1997 Loss of energetic beam ions during TAE instabilities *Nucl. Fusion* **37** 939
[12] Pinches S.D. *et al* 2006 Observation and modelling of fast ion loss in JET and ASDEX Upgrade *Nucl. Fusion* **46** S904
[13] Heidbrink W.W. *et al* 2007 Anomalous flattening of the fast-ion profile during Alfvén-eigenmode activity *Phys. Rev. Lett.* **99** 245002
[14] Ishikawa M. *et al* 2007 Confinement degradation and transport of energetic ions due to Alfvén eigenmodes in JT-60U weak shear plasmas *Nucl. Fusion* **47** 849
[15] White R.B. *et al* 2010 Beam distribution modification by Alfvén modes *Phys. Plasmas* **17** 056107
[16] García–Munoz M. *et al* 2007 NTM induced fast ion losses in ASDEX Upgrade *Nucl. Fusion* **47** L10
[17] Toi K. *et al* 2004 MHD instabilities and their effects on plasma confinement in large helical device plasmas *Nucl. Fusion* **44** 217
[18] Ogawa K. *et al* 2013 A study on the TAE-induced fast-ion loss process in LHD *Nucl. Fusion* **53** 053012
[19] Isobe M. *et al* 2006 Studies of fast-ion transport induced by energetic particle modes using fast-particle diagnostics with high time resolution in CHS *Nucl. Fusion* **46** S918
[20] Podestà M. *et al* 2009 Experimental studies on fast-ion transport by Alfvén wave avalanches on the national spherical torus experiment *Phys. Plasmas* **16** 056104
[21] Darrow D.S. *et al* 2013 Stochastic orbit loss of neutral beam ions from NSTX due to toroidal Alfvén eigenmode avalanches *Nucl. Fusion* **53** 013009
[22] Jones O.M. *et al* 2015 Measurements and modelling of fast-ion redistribution due to resonant MHD instabilities in MAST *Plasma Phys. Control. Fusion* **57** 125009
[23] Bakharev N.N. *et al* 2015 Fast particle behaviour in the Globus-M spherical tokamak *Nucl. Fusion* **55** 043023
[24] Heidbrink W.W. *et al* 2016 Interpretation of fast-ion signals during beam modulation experiments *Nucl. Fusion* **56** 112011
[25] Collins C.S. *et al* 2016 Observation of critical-gradient behavior in Alfvén-eigenmode-induced fast-ion transport *Phys. Rev. Lett.* **116** 095001
[26] Heidbrink W.W. *et al* 2017 Fast-ion transport by Alfvén eigenmodes above a critical gradient threshold *Phys. Plasmas* **24** 056109
[27] Ghantous K. *et al* 2012 1.5 D quasilinear model and its application on beams interacting with Alfvén eigenmodes in DIII-D *Phys. Plasmas* **19** 092511
[28] Waltz R.E. and Bass E.M. 2014 Prediction of the fusion alpha density profile in ITER from local marginal stability to Alfvén eigenmodes *Nucl. Fusion* **54** 104006
[29] Waltz R.E. and Bass E.M. 2015 Development and validation of a critical gradient energetic particle driven Alfvén eigenmode transport model for DIII-D tilted neutral beam experiments *Nucl. Fusion* **55** 123012
[30] Austin M.E. and Lohr J. 2003 Electron cyclotron emission radiometer upgrade on the DIII-D tokamak *Rev. Sci. Instrum.* **74** 1457
[31] Van Zeeland M.A. *et al* 2016 Electron cyclotron heating can drastically alter reversed shear Alfvén eigenmode activity in DIII-D through finite pressure effects *Nucl. Fusion* **56** 112007
[32] Zhu Y.B. *et al* 2012 Compact solid-state neutral particle analyzer in current mode *Rev. Sci. Instrum.* **83** 10D304
[33] Muscatello C.M. *et al* 2010 Extended fast-ion D-alpha diagnostic suite on DIII-D *Rev. Sci. Instrum.* **81** 10D316
[34] Heidbrink W.W. *et al* 2011 A code that simulates fast-ion D-alpha and neutral particle measurements *Commun. Comput. Phys.* **10** 716
[35] Heidbrink W.W. *et al* 1997 Measurements of the neutron source strength at DIII-D *Rev. Sci. Instrum.* **68** 536
[36] Fisher R.K. *et al* 2010 Scintillator-based diagnostic for fast ion loss measurements on DIII-D *Rev. Sci. Instrum.* **81** 10D307
[37] Van Zeeland M.A. *et al* 2006 Radial structure of Alfvén eigenmodes in the DIII-D tokamak through electron cyclotron emission measurements *Phys. Rev. Lett.* **97** 135001
[38] Gorelenkov N.N. *et al* 1999 Fast particle finite orbit width and Larmor radius effects on low-n TAE excitation *Phys. Plasmas* **6** 2802
[39] White R.B. *et al* 2010 Particle distribution modification by low amplitude modes *Plasma Phys. Control. Fusion* **52** 045012
[40] White R.B. 2011 Modification of particle distributions by magnetohydrodynamic instabilities II *Plasma Phys. Control. Fusion* **53** 085018
[41] Podestà M. *et al* 2014 A reduced fast ion transport model for the tokamak transport code TRANSP *Plasma Phys. Control. Fusion* **56** 055003
[42] Meneghini O. *et al* 2015 Integrated modeling applications for tokamak experiments with OMFIT *Nucl. Fusion* **55** 083008
[43] Sheng H. and Waltz R.E. 2016 Prediction of the fusion alpha density profile in ITER from local marginal stability to Alfvén eigenmodes *Nucl. Fusion* **56** 056004
[44] Pace D.C. *et al* 2017 Control of power, torque, and instability drive using in-shot variable neutral beam energy in tokamaks *Nucl. Fusion* **57** 014001